ADVANCED FUNCTIONAL MATERIALS
www.afm-journal.de

Novel Defense Mechanisms in the Armor of the Scales of the "Living Fossil" Coelacanth Fish

Haocheng Quan, Wen Yang, Eric Schaible, Robert O. Ritchie,* and Marc A. Meyers*

Here, experiments and analysis revealing the unique defense mechanisms of the coelacanth, a lobe-finned fish termed a "living fossil", are reported, as it was considered to be extinct until 1938, but extant for 400 million years. This defense is provided by primitive elasmoid scales having a rare double-twisted Bouligand structure of lamellae which provides extraordinary resistance to deformation without failure. Distinct from other elasmoid scales, the collagen fibrils in the coelacanth fish scales form bundles which are embedded in a matrix comprising fibers arranged perpendicular to the layered (double-twisted Bouligand) structure that provide added rigidity and resistance to deformation. Using in situ synchrotron small-angle X-ray scattering during uniaxial tensile testing, the deformation mechanisms of the collagen are identified in terms of fibril stretching, reorientation, sliding, bending, and delamination. The unique structure of the coelacanth scales, distinct from modern elasmoid scales such as the carp, provides a variety of mechanisms to arrest cracking, making it an outstanding damage-tolerant material to resist predator attacks.

1. Introduction

Through the intricate and ingenious manipulation of structures consisting of primarily minerals and biopolymers organized hierarchically, many natural materials manifest a combination of strength, toughness and light weight that are invariably mutually exclusive in synthetic materials.[1,2] The integumentary skeletons of fish, in the form of their scales, represent an excellent example of how nature evolves to afford an effective protection for the fish in its living environment.[3–5] Ancient fish were armored with large juxtaposed plates which provided a protective shield but also impeded their movement and locomotion.[6,7] Further evolution led to these large plates separating into imbricated smaller ones; a representative that still exists today is the ganoid scale.[3] It possesses very thick mineral layers that can provide outstanding penetration resistance but the rigid individual units and small degree of imbrication severely compromise the flexibility of the fish body.[6,8–11] With the further evolution, the elasmoid scales appeared, which are the prevailing type of fish scales today.[3] Much more compliant, they possess a dramatically reduced mineral layer and laminate inner core composed of non-mineralized or slightly mineralized collagen fibrils.[12–14] All the well-studied elasmoid scales exhibit an arrangement of the collagen fibrils that follows an orthogonal or twisted plywood structure (also called the "Bouligand-type" structure), which can accommodate the imparted deformation through fibrous lamellae rotation, fibril straining, and interfibrillar sliding.[15–20] Here, we present a primitive type of elasmoid scale with a unique structure that is quite distinct from the prevailing current elasmoid fish scales. We show that this scale can adapt to the loads associated with predator attacks through a suite of novel deformation mechanisms. Such a primitive type of scale is from the "living fossil" coelacanth fish.

The coelacanth, one of the two living groups of lobe-finned fish (sarcopterygians), was thought to be extinct since the Late Cretaceous period (70 Myr), yet was discovered again in South Africa in 1938.[21–23] The discovery of a living coelacanth was considered one of the most important zoological findings of the 20th century, since it is thought to belong to the transitional group in the evolution from aquatic creatures to terrestrial tetropods.[24] The coelacanth live in the Indian Ocean at a depth of typically ≈180 m, where fish are usually not as heavily

H. Quan, Prof. M. A. Meyers
Materials Science and Engineering Program
University of California
San Diego, CA 92093, USA
Dr. W. Yang, Prof. M. A. Meyers
Department of Mechanical and Aerospace Engineering
University of California
San Diego, CA 92093, USA
E-mail: wyang8207@gmail.com
Dr. W. Yang, Prof. R. O. Ritchie
Materials Sciences Division
Lawrence Berkeley National Laboratory
Berkeley, CA 94720, USA
E-mail: roritchie@lbl.gov
E. Schaible
Advanced Light Source
Lawrence Berkeley National Laboratory
Berkeley, CA 94720, USA
Prof. R. O. Ritchie
Department of Materials Science and Engineering
University of California
Berkeley, CA 94720, USA
Prof. M. A. Meyers
Department of NanoEngineering
University of California
San Diego, CA 92093, USA
The ORCID identification number(s) for the author(s) of this article can be found under https://doi.org/10.1002/adfm.201804237.

DOI: 10.1002/adfm.201804237

armored as the ones inhabiting shallower fresh water.[25–28] However, since it was first discovered by the South African museum official Margorie Courtenay-Latimer, its shiny hard armor-like scale has attracted considerable attention.[29] In this study, we characterized its intricate and ingenious structure, that of bundled collagen fibrils which follow a unique form of a double twisted Bouligand-type pattern comprised of orthogonal bilayers embedded in a through-the-thickness collagenous matrix. Our tensile tests of intact and notched samples indicate that this fibrous hierarchical structure can not only accommodate the excessive deformation by delocalizing an imposed load and dissipating any excessive energy, but also can effectively arrest any local fractures, thereby enhancing the toughness of the scale both intrinsically and extrinsically. Various toughening mechanisms including crack deflection, fiber reorientation, twisting, stretching, delamination, and the deformation of fibrous matrix are identified by *post-mortem* scanning electron microscopy (SEM) observation under both in situ and ex situ loading. We also applied in situ synchrotron small-angle X-ray scattering (SAXS) techniques for real-time analysis of mechanical tensile tests on bulk scale samples to reveal the novel deformation and toughening mechanisms within the collagenous inner core in the scale of this ancient creature.

2. Results and Discussion

The entire body of the coelacanth (*Latimeria chalumnae*) is covered by armor-like scales with a bright metallic blue color when the fish is alive, although these fade to brown color after preservation (**Figure 1**a).[21,25,30] The imbricated scales (Figure 1b) have a very rough surface exposed to the environment, occupying around one third of the entire scale (inset in Figure 1b), with the overlapped part deeply inserted into the fish skin, similar to the other typical elasmoid ones such as carp scales (Figure 3a,b). Micro-computed tomography (micro-CT) shows the exposed part to be more mineralized than the overlapped part (Figure 1c), with numerous odontodes scattered on it (Figure 1d). A micro-CT scan of an isolated odontode (Figure 1e) indicates that it is composed of a denticle on top of a star-like base which anchors it to the radial ridges. The cross-sectional view of the scan (Figure 1f) reveals its hollow structure with the shell being highly mineralized. The schematic in Figure 1g fully illustrates the tooth-like structure of the odontode, as carefully characterized in refs. .[31,32] Specifically, it is composed of dentin, with a 3D pulp cavity inside, created on the top of a bony base with the surface covered by a thin layer of enamel. All the odontodes are partially embedded in the dermis, which implies that their prime function is to anchor the scales in the integument.[32] The mineral ridges radiating from the apex of the scale (Figure 1h) are regularly arranged with almost equivalent separated space in both the overlapped and exposed parts of the scale (Figure 1i). The regions between the mineral ridges that are located just above the inner layer can be regarded as the head of the mineralization of the inner layer; they are covered by spherical mineralized spherules. The openings of the vascular canals are also observed on the regions between the ridges, consistent with the previous observations.[31,32]

Beneath the thin surface layer is the major component of the scale, the isopedine,[31] comprising a laminated collagenous tissue with a twisted "plywood" structure (**Figure 2**a). Different from the common elasmoid scales of other modern teleosts such as carps, in which each lamella is directly composed of individual collagen fibrils (**Figure 3**c), the collagen fibrils in the coelacanth scale are tightly packed into distinct bundles and the fiber bundles (FBs) are aligned parallel in each lamella (Figure 2b,c). Additionally, the arrangement of the collagenous lamellae does not simply follow the stair-case pattern of a typical "Bouligand-type" structure, which commonly appears in other elasmoid scales (Figure 3d). In the coelacanth scale, the FBs in the adjacent two lamellae, whose orientations are marked with arrows in Figure 2d, form an orthogonal bilayer, as shown in the inset; the units of orthogonal bilayers progressively rotate through the whole thickness in stair-case pattern, forming what is known as a double-twisted "Bouligand-type" structure.[21] The spaces between the FBs are filled with fibrils perpendicular to the laminate structure, along the thickness direction (Figure 2e), which are referred here as interbundle fibrils (IBFs). They are much more loosely packed yet are aligned more randomly than the fibrils in the FBs. We performed transmission electron microscopy (TEM) on the scale to confirm that the orthogonal arrangement of adjacent lamellae in one bilayer and the penetration of the IBFs through several layers provides a wrap for the FBs, thereby forming a matrix that is the binding material (Figure 2f). The IBFs are also collagen, as shown by characteristic banded patterns (Figure 2g). Such a distinct interbundle matrix is unique to coelacanth scales; the other common elasmoid scales have only few perpendicular fibrils (shown by the arrow in Figure 3f) barely forming a matrix (Figure 3e,f). Using this detailed characterization of the outer and inner layers of the scale, a complete structure of the coelacanth scale can be revealed in terms of three principal components:

a) The collagen fibrils form bundles that organize into orthogonal bilayers, the bilayer arrangement following a "Bouligand-type"pattern (Figure 2h);
b) Loosely packed IBFs form perpendicular to the Bouligand layers and extend through the thickness of inner layer (Figure 2i); they wind around these bundles to act as a binding material to confine the FBs in the lamellae;
c) The surface is covered by a ridged thin mineral layer (Figure 2j).

This complex yet fascinating hierarchical structure significantly enhances the toughness, i.e., resistance to penetration and fracture, of the coelacanth scale, which is vital for protecting the body of the fish from predators. In order to verify this, a penetration test using a shark tooth was performed on two unattached but overlapped coelacanth scales located on a base of a slab of fresh fish flesh. The resulting force versus displacement curve, shown in **Figure 4**a, indicates periodic drops in the curve which are associated with the penetration of different layers of the scale. The tooth penetrated through the top scale and lifted it up, but left the bottom scale largely undamaged. After the test was performed multiple times, it was clear that the actual penetration damage avoided the actual location of the odontodes and always occurred between them (Figure 4b). Though a large penetration displacement was involved in the

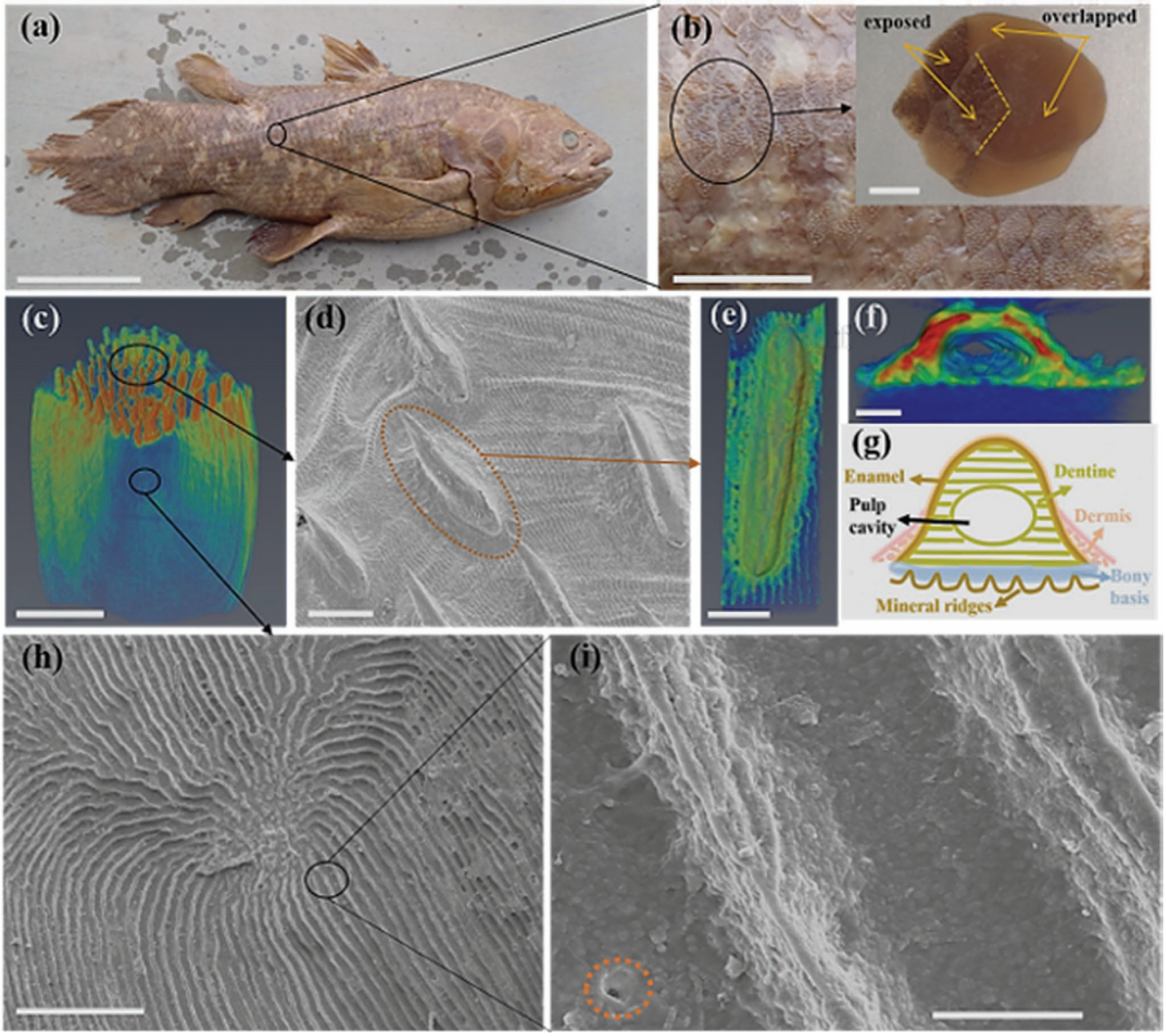

Figure 1. Surface morphology of the scale. a) The entire coelacanth fish body is armored with scales. They are shinny dark blue when the fish is alive and the color fades after the fish is dead (scale bar 20 mm). b) Scales are imbricated: the posterior part, which is around 1/3 of the whole scale, has very rough surface and is exposed to the environment. (scale bar, 50 mm). The anterior part is overlapped by the neighboring scales and inserted deeply in the fish skin (see inset, scale bar, 10 mm). c) Micro-CT scan of a scale. The mineralization of the exposed part is much higher (red) than the overlapped part (scale bar, 10 mm). d) SEM image of the exposed part (scale bar, 500 µm). The odontode is circled with a dotted line. e) Micro-CT scan of an isolated odontode (scale bar, 200 µm). The odontode is composed of two parts: a denticle on the top and a star-like base. f) The cross-section of the micro-CT scan of an isolated odontode shows the highly mineralized outer layer (red) and a pulp cavity inside (scale bar, 100 µm). g) Schematic of the structure of the odontode. h) The SEM image of the scale center reveals that radial ridges originating from the apex are arranged more regularly (scale bar, 200 µm). i) Higher magnification SEM shows abundant corpuscles and a few openings of vascular canals (circled with dotted line) between the mineral ridges (scale bar, 10 µm).

scale with a small thickness of ≈0.5 mm, the damage was localized with the remaining area left undamaged. Within a single scale, cracks initiated in the outer layer propagated but were arrested by other cracks, as shown by the circles in Figure 4b. The inner layer was damaged locally and became exposed from the damage to the outer layer. However, with SEM examination, it was apparent that the collagen fibrils in this inner layer were indeed stretched and some were delaminated, but with little other overt damage (Figure 4c). Under extreme penetration displacements into the scale, the inner collagenous layer played a role of tough base under the tension force. Using the concept of a harder outer layer to resist penetration with a more ductile lower layer to accommodate the excessive strain, the tough collagenous lower layer served to localize the outer layer cracking and avoid catastrophic separation.

To re-evaluate the effect of the collagenous layer, the fracture toughness was estimated using pre-cracked compact-tension specimens loaded between anti-buckling plates. Extension of

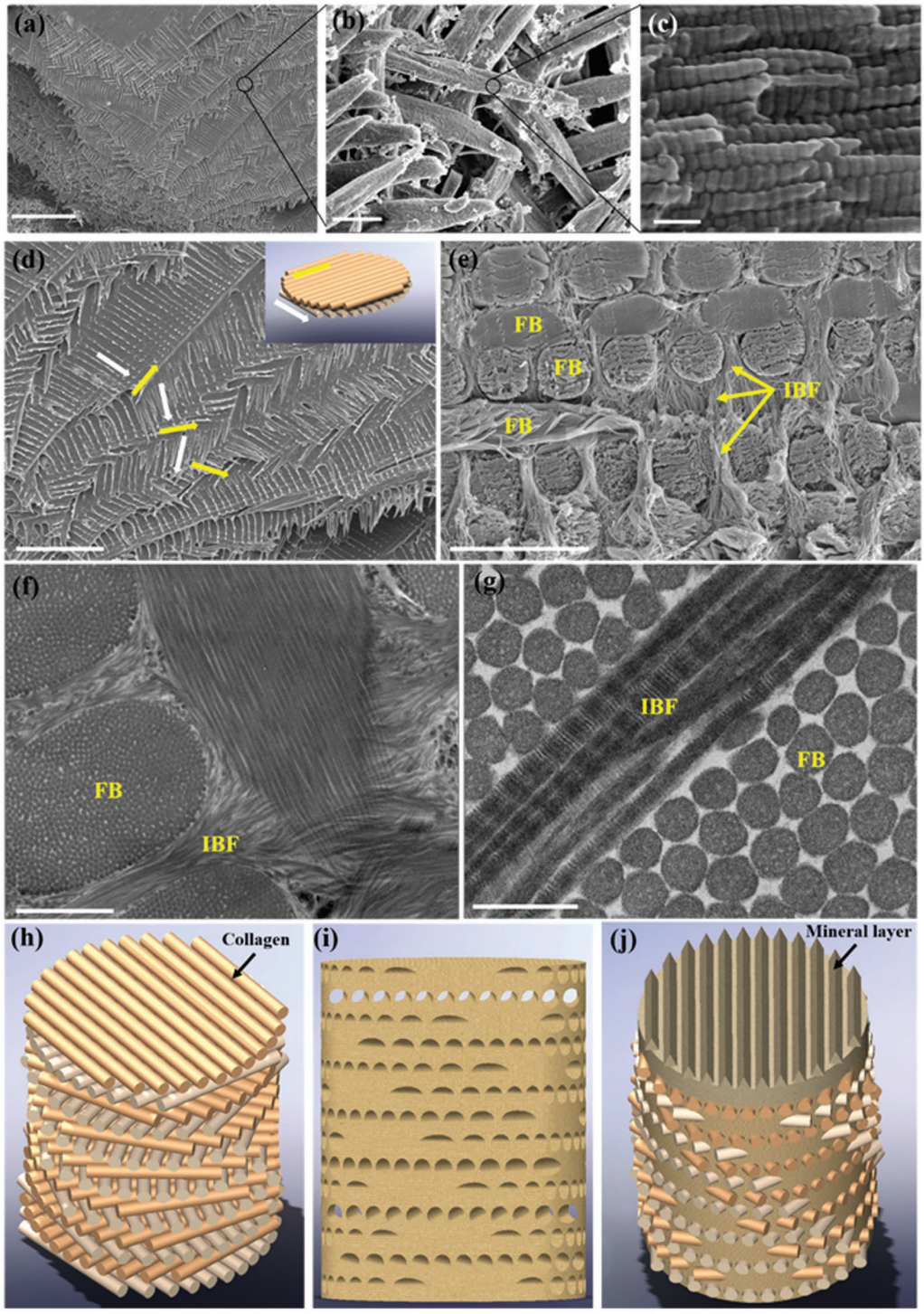

Figure 2. Structure of the inner layer of the coelacanth scale. a) The oblique fractured surface reveals the "plywood" arrangement of laminate inner layer (scale bar, 100 μm). b) Each lamella is composed of collagen FBs arranged in parallel (scale bar, 5 μm). c) The bundle is formed by the tightly packed collagen fibrils (scale bar, 200 nm). d) The close-up view of oblique fractured surface. The orientations of the collagen FBs in three successive layers are marked with arrows. The orientations in adjacent two layers are almost perpendicular to each other and the schematic of such arrangement is shown in the inset (scale bar, 50 μm). e) Vertical cross-sectional view shows that the spaces between the FBs are filled with IBFs, which go through the whole thickness of the inner layer, binding the lamellae (scale bar, 10 μm). f) TEM image of two adjacent collagenous lamellae showing that the loosely packed IBFs wrap the collagen bundles (scale bar, 2 μm). g) The characteristic band pattern of collagen fibril is clearly shown in the high magnification TEM (scale bar, 200 nm). h–j) Schematics of the structure of the coelacanth scale, (h) the double twisted Bouligand structure with orthogonal bilayers progressively rotating throughout the whole thickness, (i) the matrix composed of IBFs to hold such a system with (j) the top covered by a mineralized outer layer.

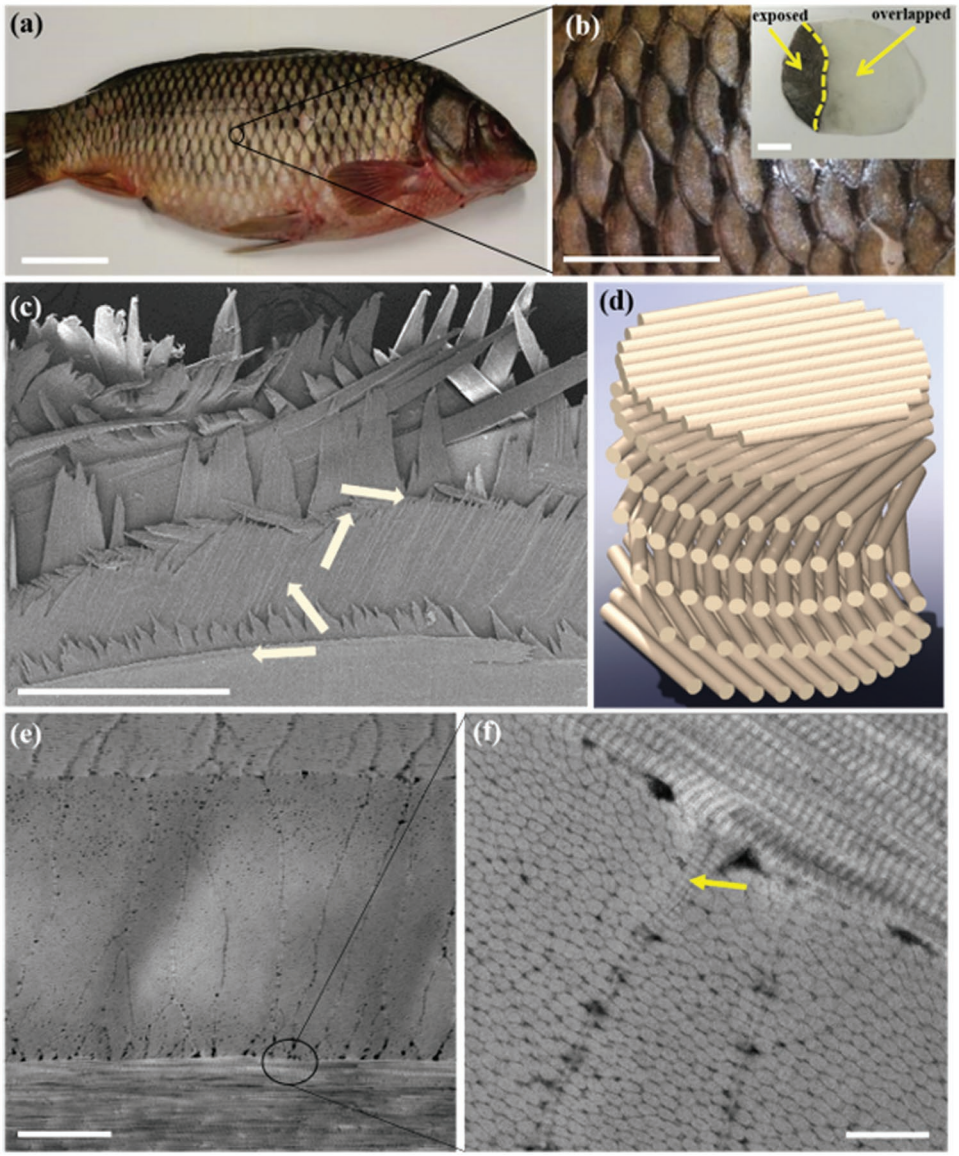

Figure 3. Structure of the inner layer of carp scales. a) Common carps are armored with typical modern elasmoid scales (scale bar 100 mm). b) The carp scales are imbricated in a similar way as the coelacanth ones (scale bar, 50 mm; scale bar in inset, 10 mm). c) SEM image of a carp scale fractured in liquid nitrogen (scale bar, 200 µm). d) Schematic drawing of typical single twisted Bouligand structure. e, f) TEM images of carp scales with different magnifications show only a few IBFs (indicated by the arrow) running through the thickness direction which do not form the distinct matrix (scale bar 2 µm, 400 nm, respectively).

the fully hydrated and pre-cracked specimen resulted in the crack-tip opening and blunting. This was followed by distinct fiber bridging as the crack started to propagate (**Figure 5**a–c). The estimated fracture toughness K_{Ic} of coelacanth scales was found to be 4.9 ± 1.5 MPa·m$^{1/2}$, which is not particularly impressive yet is still comparable to the toughness of other elasmoid scales (see, for example, Dastjerdi et al.[14]). Nevertheless, this value is high compared to many other biological materials. The fracture toughness value is not as high as we expected from this complicated structure; however, one must recognize that the tested coelacanth specimens have been preserved in isopropanol for 45 yr, which clearly resulted in some deterioration in their mechanical properties. Such an effect is consistent with the noticeable reduction in strength of common carp scales after two years of preservation (as described in Figure S1, Supporting Information). In other words, fresh coelacanth scales likely have a somewhat higher toughness.

The in situ SEM sequence of images during the loading of a pre-cracked specimen in Figure 5 (d–f, g–i) reveals the details of the toughening mechanisms. The crack deflects as soon as it starts to propagate (Figure 5d) with the collagen fibers bridging across the crack surfaces (Figure 5e). The FBs tend to rotate and deform as a unit; bundles first separate from their neighboring bundles and then delamination of the internal fibrils occurs within each bundle (shown by the arrow in Figure 5f). With further extension, fibers/fibrils along the propagating direction of the crack delaminate and pull-out, with associated necking prior to their fracture (shown by arrows in Figure 5h).

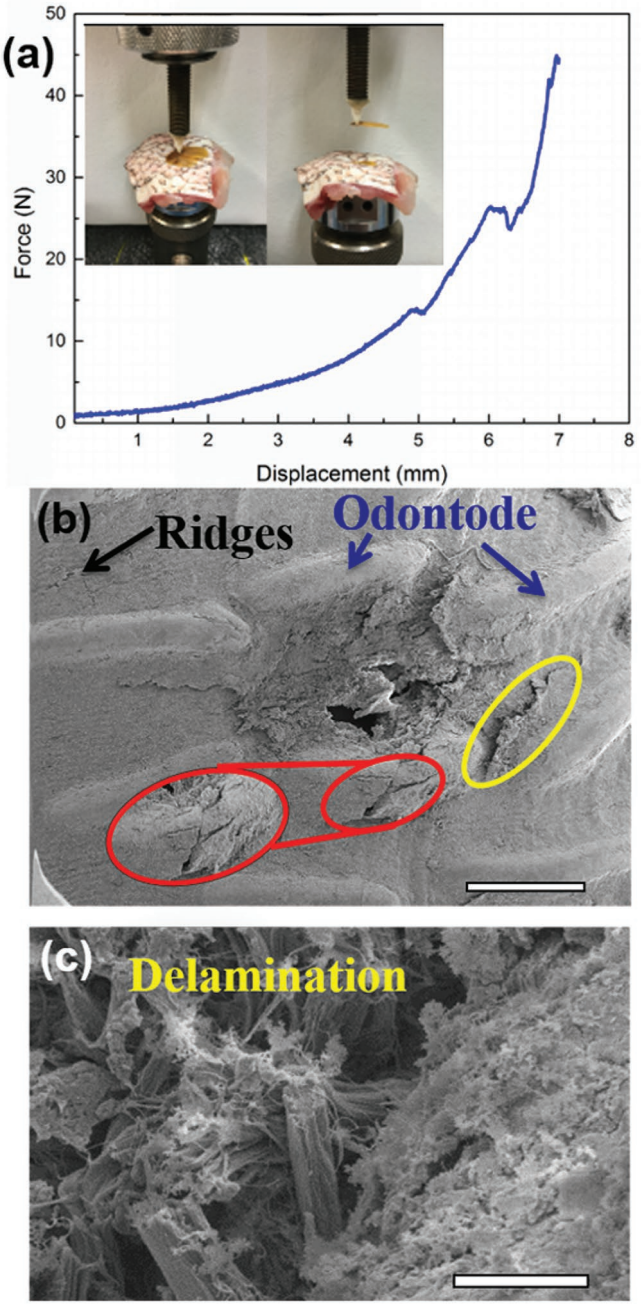

Figure 4. Penetration of a coelacanth scale by a shark tooth. a) Force versus displacement plot with the images of loading and unloading;[9] b) the top scale with the penetration damage. Note that the damage is localized among the odontodes (scale bar, 500 µm). c) The collagen fibrils were stretched, delaminated, and curled after fracture (scale bar, 20 µm).

Most of the fibers fractured in a brittle fashion, possibly aided by dehydration from the vacuum inside the in situ SEM.

Most biological materials lose some degree of their deformability in the dehydrated state. Collagen-based materials, such as the fish scales, are no exception and sacrifice their ductility when they are not fully hydrated. Due to dehydration of the samples (≈50% dehydration from the preserved samples) in the in situ SEM tests, there was no clear observation of crack blunting and fiber bridging before the initiation of cracking, although these features were clearly evident in the ex situ tensile tests (Figure 5a–c). Consequently, to further demonstrate the tough nature of the coelacanth scales, we also performed uniaxial tensile tests on 3-mm wide dog-bone-shaped specimens containing each a 1.5-mm deep notch, as indicated in the inset of **Figure 6**a. The average measured tensile strengths (and their variation) of coelacanth scales in the longitudinal and transverse directions were 45.5 ± 4.9 and 46.9 ± 12.7 MPa, respectively. The slight variation in the thickness of the samples along the gauge length of the test samples had little effect on the measured strength—indeed, strength values were quite consistent; however, since the coelacanth scale has a shorter transverse length with relatively small thickness close to the edge, the thickness of the samples had a slightly larger variation on the transverse samples where strength values were found to have a higher standard deviation (21.7% of the average value, 12.7 MPa). Compared with the tensile results of the unnotched samples (Figure 6g), the pre-notched samples (Figure 6a) showed very little notch-sensitivity, i.e., the strength and ductility did not decrease dramatically with the presence of crack; rather, the notched scales displayed similar tensile mechanical properties to the unnotched specimens. As more mechanistic information can be gleaned from such tension tests of pre-cracked hydrated samples, we loaded fully hydrated samples in tension to cause propagation (without a final failure) of a crack, prior to ex situ SEM observation. Based on the SEM imaging of the crack-tip region (Figure 6b–f), we identified several mechanisms associated with deformation and fracture in these scales:

a) shear failure of the mineral (Figure 6e);
b) deformation of the FBs which become twisted, distorted/bent, and delaminated with the stretching and reorientation of the fibrils (Figure 6d);
c) crack bridging by the stretched FBs (Figure 6d,f);
d) delamination and relaxation of the fractured FBs further away from the crack-tip region (Figure 6c,f);
e) the matrix of IBFs acts to constrain the FBs, as shown in Figure 6(h,i), although the IBFs delaminate after the FBs are pulled out from the matrix.

Accordingly, based on these observations, we conclude that the double Bouligand structure and the matrix of IBFs are the keys to generating the toughness of the scales. The mineral and collagen utilize different mechanisms to avoid catastrophic failure; while the external load is increasing, the collagen fibrils are continuously stretched but the mineral stops shearing and any cracks are arrested by the resultant bridging. More micro-deformation mechanisms are involved in this procedure, including crack deflection in the mineral layer, delamination between collagen bundles, and separation at the relatively weak interfaces between the collagen bundles and the IBFs. Note that some of the IBFs extend directly into a collagen lamella, all of which serve to confer toughness to the coelacanth scales. At relatively low tensile strains, the IBFs deform, due to the Poisson effect, and function to hold the collagen fibrils together to prevent delamination; at larger strains, it is possible that they could generate stress concentrations, although without the constraining effect of the IBFs, the collagen lamellae would delaminate and be largely separated at an early stage; in other words, the relatively weak interfaces can lead to enhanced

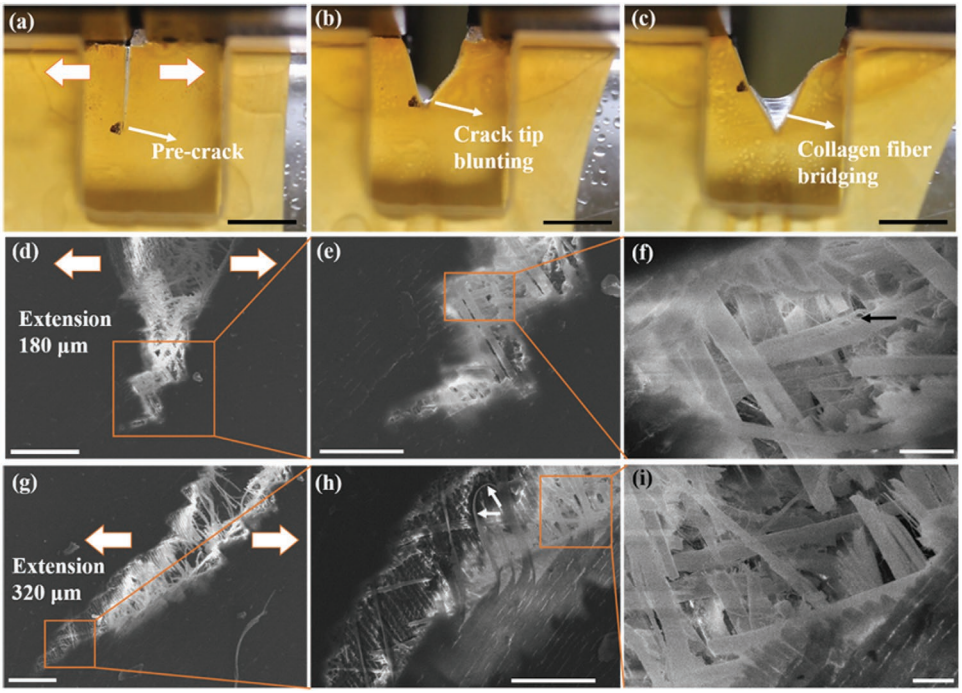

Figure 5. Fracture toughness test and crack propagation process. a) The set-up of the fracture toughness test with anti-buckle plates (scale bar, 3 mm). b,c) The images at different stages during the fracture toughness test (scale bar, 3 mm). b) The crack tip opens and becomes blunt first; and c) with further extension, the collagen fibrils are pulled out and form bridges behind the crack tip. d–i) In situ SEM observation of crack propagation of a dehydrated coelacanth scale under tension load. d–f) The crack-tip region when the scale has been tensile extended by 180 µm (scale bar, 100, 50, and 10 µm, respectively). After the initiation of cracking, the crack deflects in a zig-zag pattern, with collagen FBs being stretched and bridging behind the crack tip. Some fibers were delaminated (shown by the arrow). g–i) The crack-tip region when the scale is extended by 320 µm (scale bar, 100, 50, and 10 µm, respectively). g) More fibers are pulled out and fractured, h) fibers aligned along the crack propagation direction are delaminated with necking prior to fracture (shown by arrows), and i) behind the crack tip, more fibers in different orientations are fractured.

toughness by enabling sliding between the matrix (IBFs) and collagenous lamellae which increases the deformability of the entire scale. Additionally, intense deformation at the nanoscale, associated with the bending, twisting, stretching, and delamination of the fibrils in the FBs, coupled with the deformation of the collagen matrix and some degree of secondary cracking and crack deflection in the mineral layer, act *in concert* to further enhance the fracture toughness of these scales.

Based on the studies of Puxkandl et al.[33] and Gupta et al.[34] which demonstrated that high intensity X-rays can be a powerful tool to investigate the mechanical behavior of collagenous tissue, we utilized in situ SAXS during uniaxial tensile testing of the scales in the X-ray synchrotron to discern the precise deformation and toughening mechanisms in the collagenous inner layer in real time (**Figure 7**a). The X-rays interact with the regular *d*-spacing of the collagen fibrils and generate a diffraction pattern composed of numerous sets of concentric arcs[35,36] (Figure 7b). The first-order arc is closest to the beam center and represents the distance q from the center which changes inversely with the *d*-spacing of the collagen fibrils.[15,35,37] The azimuthal angle Ψ of the first-order arc follows the orientation of the corresponding collagen fibrils, with multiple orientations of collagen generating arcs that superimpose to form a Debye ring, as illustrated in Figure 7b. Therefore, by measuring the changes in q and Ψ along the first-order arcs, the strain and rotation of the collagenous lamellae and the deformation of the collagen fibrils can be tracked in real time while a tensile load is being applied on the scale (in the present experiments, the tensile loading was applied along $\Psi = 0°$). The integrated intensity distribution along the Debye ring can quantify the orientations of the lamellae due to the one-to-one correspondence between the intensity peaks in Figure 7c,d and the fibril orientation. The plot for the coelacanth scale in Figure 7c shows numerous peaks distributed with unequal separation along the azimuthal angle, suggesting that, due to the double-twisted arrangement the scheme of which is shown in the inset, the collagen fibrils in the coelacanth scales conform to many orientations with irregular distributions. The different peak heights appear to result from the bundle size gradually decreasing from the outer to the inner regions of the scale (Figure S2, Supporting Information); larger bundles containing more collagen fibrils lead to a higher diffraction intensity. Additionally, fibrils in different lamellae can arrange in a common direction repeatedly through the thickness and this can also contribute to the intensity of the peak (Figure 7c). This highlights the uniqueness of the coelacanth scale compared to the corresponding SAXS spectrum for modern elasmoid scales, e.g., for the carp scale in Figure 7d. Distinct from coelacanth scales, the carp scale has a traditional single "Bouligand-type" structure, showing five peaks with similar intensity; this indicates that the collagen fibrils in successive lamellae are arranged in a highly ordered twist configuration with an average rotation angle of 36°, the number of the collagen fibrils in each orientation being almost the same.

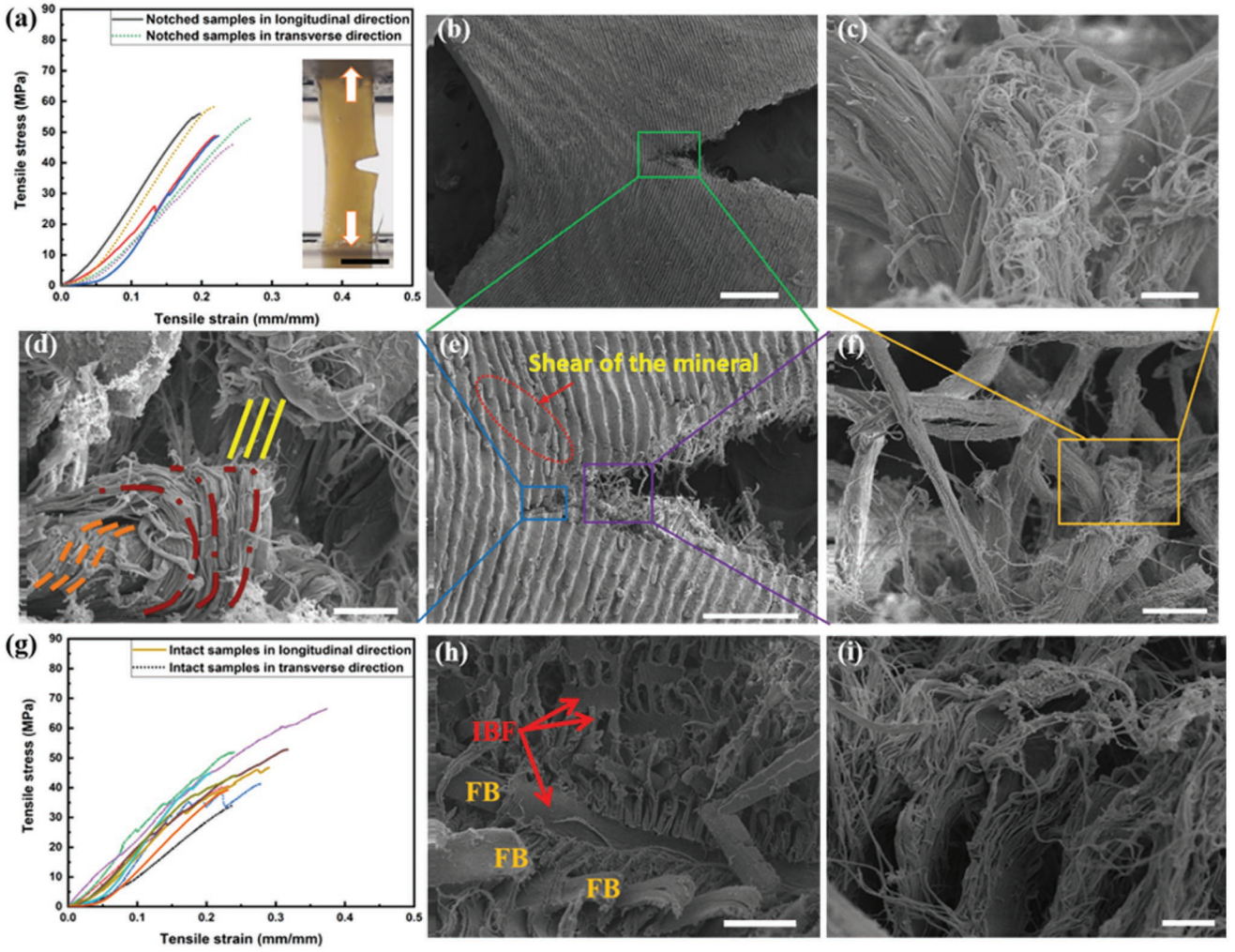

Figure 6. Mechanisms of retardation of crack formation in the scale. a) The tensile stress–strain curve of notched samples. The inset shows the blunted notch in the hydrated scale when the sample is being tensile tested (scale bar, 3 mm). b–f) The SEM images of the regions around the crack tip. b) Overview of crack propagation; region around the crack tip is boxed (scale bar, 500 µm). c) Severe stretching, delamination, and relaxation of the fibrils in the FB (scale bar, 2 µm). d) FBs close to the crack tip are bent, buckled, twisted while being stretched partially around the head of the crack. (scale bar, 5 µm). e) Close-up view of the region around the crack tip reveals secondary cracks (shear of the mineral) in the mineral layer and fibril stretching, delamination and relaxation behind the crack tip (scale bar, 200 µm). f) Close-up view of the region behind the crack tip also showing severe stretching, bending, buckling, rotation, and delamination of the bundles (scale bar, 10 µm). g) Tensile stress–strain curve of intact samples. h) Typical fracture surface after tensile failure indicates the extensive deformation of FBs and IBFs (scale bar, 20 µm). i) SEM image at higher magnification shows the squeezing, stretching and delamination of the IBF matrix (2 µm).

One highly effective toughening mechanism in fish scales is the physical rotation of collagen fibrils towards the direction of the applied tension in order to carry more of the load.[15] To investigate how the complex orientations of collagen lamellae in the coelacanth scale reorient under load, and further how the collagen fibrils deform within a matrix of loosely packed IBFs, we analyzed real-time diffraction patterns of samples cut along the longitudinal and transverse directions of the scales (Figures 7 and 8, and Figures S3–S5, Supporting Information). An example of one of these experiments showing the stress–strain curve and real time SAXS patterns taken during the tensile deformation (for five selected data points at tissue strains ε_t of 0, 0.05, 0.11, 0.16, and 0.22), is presented in **Figure 8**a. (The tissue strain here refers to the macroscopic strain in the scale sample). In the unstressed state (ε_t = 0), because of the widely distributed orientations of the collagen fibrils in coelacanth scale, the numerous concentric arcs are circular indicating that the characteristic *d*-spacing of the collagen fibrils in all lamellae is almost same, i.e., 63.5 ± 0.2 nm, as quantified from the diffraction pattern. However, with increasing applied tensile loading, the scale becomes stretched, causing the diffraction pattern to gradually change from a circular to a rectangular shape with arcs at the corners designated as "square-oval-like" shape, which is completely different from the SAXS pattern of single Bouligand structure.[15] The integrated diffraction intensity as a function of the azimuthal angle at the five tissue strains ε_t is plotted in Figure 8b, which reveals that with the increase of the applied load, the peaks between $\Psi = \pm 40°$ are gradually merged into a broad peak located along the loading direction.

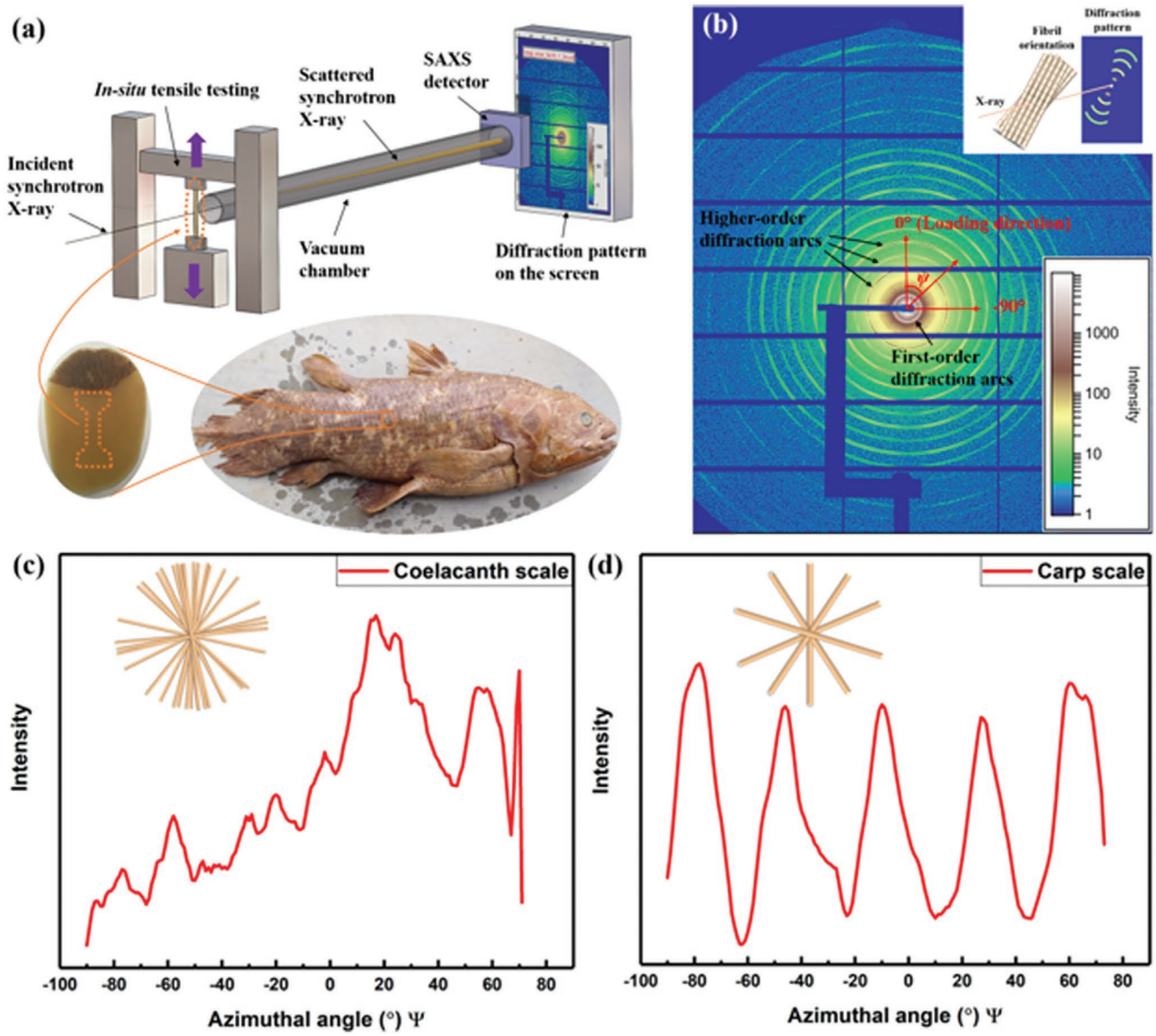

Figure 7. Experimental set-up for the in situ synchrotron SAXS during tensile tests and lamellae orientation in the scale. a) Dog-bone-shaped specimens are cut from the overlapped parts of the scales along both longitudinal and transverse directions. The scale sample is successively radiated with synchrotron X-rays in the beamline at the Advanced Light Source during the tensile tests, with the scattering patterns recorded at different stages of the deformation. b) A representative diffraction pattern of the unstressed sample shows the several sets of concentric arcs which result from the X-rays being diffracted by the collagen fibrils in the scale. These concentric arcs are generated by the periodic structure in the collagen fibrils and the orientation of each set is parallel to the alignment of one group of the fibrils. The azimuthal angle, ψ, is defined as 0° at the loading direction. c–d) The plots of diffraction intensity as a function of azimuthal angle for the (c) coelacanth scale and (d) carp scale indicate that the collagenous lamellae in the inner layer of coelacanth scale have more orientations than those in carp scale.

This suggests that the lamellae with orientations in this range gradually rotate towards the tensile orientation. Meanwhile, the peaks from $\Psi = -90°$ to $-40°$ and those from 40° to 90° gradually move away from the loading direction and display less intensity, suggesting that fewer lamellae align close to the horizontal direction. There is a continued reduction in intensity along the horizontal direction as the scale is further stretched; this is indicated by the negative peaks (dot circle) in Figure 8b, and appears to result from the opening between FBs and their early failure with separation of these lamellae. The signal between $\Psi = 70°$ and 90° is not detectable due to the experimental set-up.

Since SAXS data are statistical, in order to quantify the deformation of the collagen fibrils in detail, we divided the diffraction pattern from $\Psi = -90°$ to 70° into 17 sectors with a span of 10° to see how each orientation of collagen fibrils behaves under the tensile load. Fibers in the orientation range between $\Psi = -40°$ and 40° were significantly stretched (Figure 8c) while rotating towards the tensile direction (Figure 8b); the maximum tensile strain in the fibrils, which we measured as 0.12, was

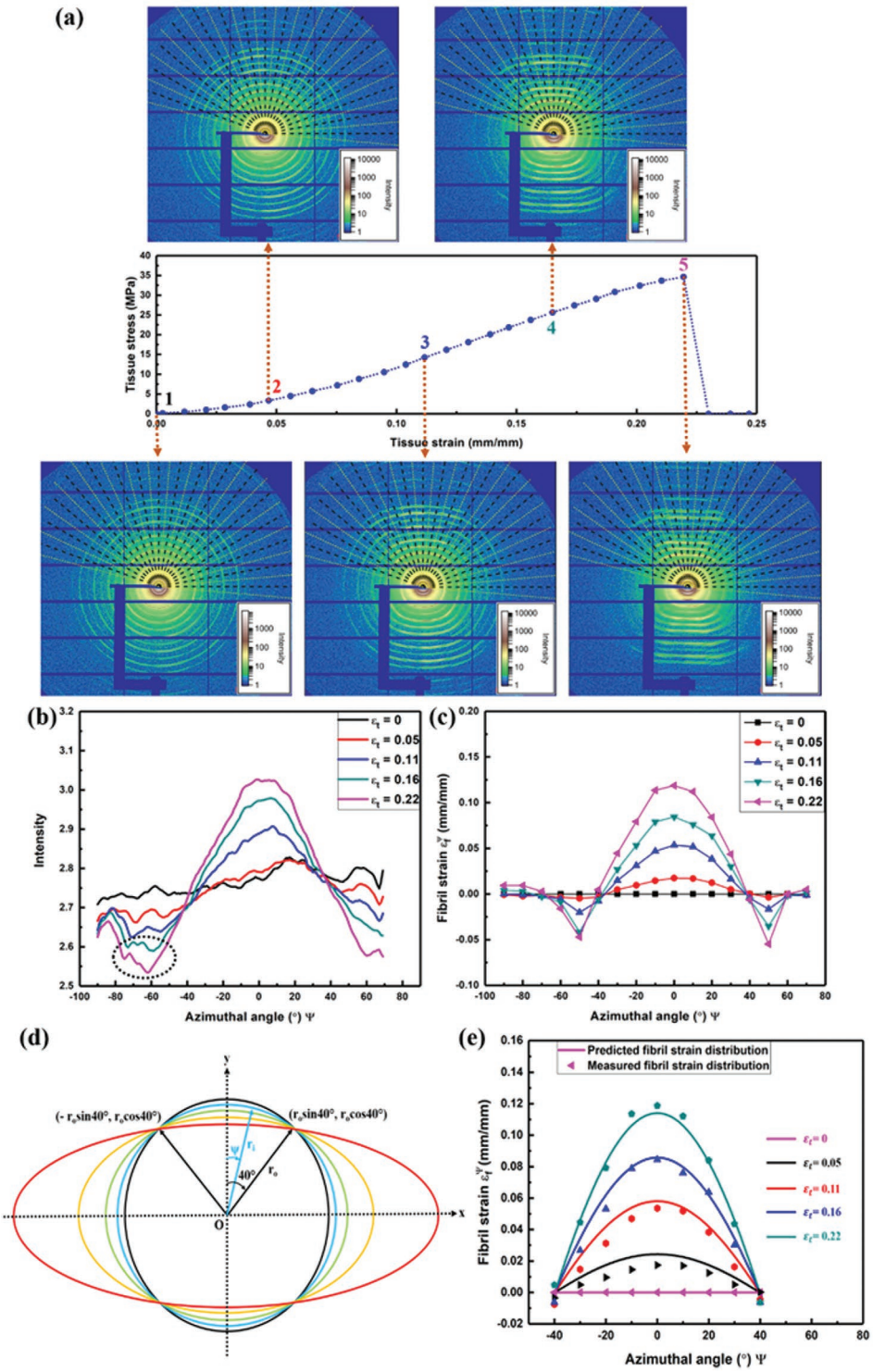

Figure 8. Rotation of lamellae and deformation of collagen fibrils in the coelacanth scales. a) The SAXS diffraction patterns of the scale at five data points (ε_t = 0, 0.05, 0.11, 0.16, and 0.22) during the uniaxial tensile test are selected to represent the in situ structural change. The shape change of the diffraction pattern indicates the inhomogeneous deformation of the fibrils in different orientations. b) Plots of diffraction intensity as a function of the azimuthal angle at the corresponding deformation stages. c) Plots of fibril strain as a function of the azimuthal angle. The fibril strain is calculated from the *d*-spacing change during the tensile test and normalized by the *d*-spacing of collagen fibrils in the original state. d) The evolution of elliptical shape of the diffraction pattern; based on the measurement from the in situ SAXS experiment, two points at $\Psi = \pm 40°$ are fixed during the change of the diffraction patterns. The black circle is the diffraction pattern at the unstressed state (circular) and the red elliptical one is at the maximum strain state. e) Evolution of fibrillar strains with azimuthal angle Ψ at different loading stages (tissue strain ε_t is shown in figure). The predicted results based on the model (continuous curves), described in the Supporting Information, are compared with experimental results (points).

located at $\Psi = 0°$, i.e., along the loading direction (Figure S3, Supporting Information). This local strain is significantly lower than the macroscopic strain applied to the entire tissue sample at failure ($\varepsilon_t \approx 0.22$), indicating that considerable inelastic ("plastic") deformation can occur in the scale by fibril shear and sliding; this provides the basis of ductility in the coelacanth scale. Specifically, along with the lamellae rotating towards the loading direction, the collagen fibrils in these lamellae are also being stretched with concomitant sliding, which represents potent mechanisms of inelasticity. At $\Psi = \pm 40°$, the fibril strain is zero, and all deformation is accommodated by such fibrillar sliding; this is close to the direction of maximum shear stress. The gradual change from circular to rectangular shape in the diffraction rings can be explained by the function of the IBFs. Distinct from the other elasmoid fish scales with single Bouligand structure,[15] the intensity of fibrils located between $\Psi = -30°$ and 30° (excluding those along the tension direction) is still high with a large value of q; this indicates that many collagen fibrils in this range experience less strain as they are constrained by the interbundle fibrils from rotating further towards the tensile direction. Under the tensile load, the collagen FBs can be microscopically compressed by the closing of the interbundle matrix. Both of these mechanisms, which cause the SAXS pattern to display compression of the collagen fibrils at around $\Psi = \pm 50°$ (Figure 8c), are a characteristic of coelacanth scales in both the longitudinal and transverse directions, as analyzed in Figures S4 and S5 in the Supporting Information.

In coelacanth fish scales, there is clearly a hierarchy of toughening mechanisms which is developed over a range of structural dimensions, namely, the interbundle matrix at the near macro-scale, the double-twisted Bouligand collagen lamellae and collagen FBs at the microscale, and the nano-scale collagen fibrils within these bundles. In addition to the ductility generated by the stretching and sliding of the collagen, the role of the unique IBFs matrix is critical here, as without this microstructural feature, most collagen fibrils would rotate towards the tensile direction but then would readily delaminate (this would appear as a sharp short arc along the tensile direction in the SAXS patterns). We have developed an analytical model to describe this complex evolution of strain, which expresses the fibril strains in terms of evolving concentric ellipses (Figure 8d). This model is derived in the Supporting Information, and provides a satisfactory match between predicted values of fibrillar strain distribution (continuous values) and our experimental results (points), as shown in Figure 8e. This model might also be applied to other collagenous materials with same double-twisted Bouligand structure. The latter structure though is uncommon but the out-plane fibrous matrix is a key to its effectiveness. If there were other biological or bio-inspired materials having similar structure as the coelacanth scale—we are unaware of any except the Australian lungfish—then the evolution of fibrillar strain within certain range might well follow the model that we constructed.

3. Conclusions

In summary, we have carefully characterized the detailed structure of the coelacanth scale: the loosely packed IBFs generate a matrix that acts as a binding material to confine the FBs in the lamellae into a double-twisted Bouligand arrangement with the external surface covered by a ridged thin mineral layer. Such a hierarchical fibrous structure can effectively arrest crack propagation, constrain the delamination of the collagen fibrils, and enhance the stretching and sliding along the tension direction with large strain, which renders the coelacanth scale a tough material to resist predatory attacks. Mechanical tensile testing coupled with SEM and in situ synchrotron SAXS revealed its unique deformation mechanisms. The lamellae with orientations close to the tensile axis rotate towards the loading direction along with stretching and sliding of the fibrils to adapt to the applied load, as described by the constitutive equation developed in the Supporting Information. The fibrils oriented far from the tensile axis (beyond $\Psi = \pm 40°$) rotate away from the loading direction. Within this range, they are non-uniformly deformed in compression as they are affected by the constraint of the matrix which forces the collagen FBs to bend and twist; this represents a manifestation of the Poisson's ratio effect (lateral contraction). The sophisticated hierarchical structure of the coelacanth scale, with its double-twisted Bouligand structure, is quite unique, as compared with the modern elasmoid scales in teleosts, and provides an excellent protective function for this "living fossil" fish. Such a unique structure may well inspire innovative designs for new high-performance structural materials.

4. Experimental Section

Materials: The scale samples were obtained from a coelacanth (*Latimeria chalumnae*) with a length of 950 mm in the Marine Vertebrate Collection of Scripps Institution of Oceanography, University of California, San Diego; the fish specimen was collected from Grand Comore Island in 1973 and has been kept in 80% isopropanol. The length of scales varied from 20 to 40 mm; they were peeled off from the *linea lateralis* below the anterior dorsal fin, caudal peduncle region and caudal region on the fish body.

Sample Preparation and Structural Characterization: The structure of the scales, the fracture surfaces after tensile testing and the crack propagation samples were all characterized in an FEI SFEG ultrahigh-resolution SEM (FEI, Hillsboro, OR). Before the structural characterization, the samples are first immersed in 2.5% glutaraldehyde for 1 h to fix the structure and then dehydrated with an ascending series of ethanol (30, 50, 70, 90, 95, and 100 vol.% twice). To obtain the oblique fracture surface, the scale was immersed in liquid nitrogen for 30 s and then immediately fractured using forceps. The fractured samples were immersed in ethanol and dried in a critical point dryer (Auto Samdri 815A, Tourisms). All dried samples, including the fractured samples after tensile testing, were sputter coated with iridium using an Emitech K575X sputter coater (Quorum Technologies Ltd.) before SEM observation. Micro-CT scans were conducted on air-dried samples in a Zeiss Versa 510 X-ray microscope (Zeiss, German).

To prepare the TEM samples, the coelacanth scales were first cut into small strips, with a length of 4 mm and a width of 2 mm, and then immersed into 2.5 vol% glutaraldehyde in 0.15 M sodium cacodylate buffer (pH 7.4) for 50 min to fix the structure. The fixed specimens were stained in a 1 vol.% OsO_4 solution with 8% potassium ferrocyanide in 0.5 M sodium cacodylate buffer for 12 h at room temperature. The scales were then stained with 2 vol.% aqueous uranyl acetate for 12 h and subsequently dehydrated with an ascending ethanol series (50, 70, 90, and 100% twice), followed by a 1:1 ratio of 100% ethanol and 100% acetone, and finally 100% acetone. The fully dehydrated specimens were embedded in Spurr's low viscosity resin and polymerized at 60 °C for

48 h. The resulting blocks were then sectioned parallel to the vertical cross-section, prior to the generation of ultrathin slices, with thickness of 80–100 nm, using a Leica Ultracut UCT ultramicrotome (Leica) and a Diatome diamond knife (Diatome). Ultramicrotomed sections were then placed on copper grids for TEM observation, and post stained with Sato lead for 1 min before final examination. TEM images were taken on FEI Technai 12 (Spirit, 120-kV) TEM (FEI, Hillsboro, OR).

Penetration Test: Two coelacanth fish scales were immersed in water for more than 48 h prior to testing. A fresh fish flesh was used as a base with the overlapped coelacanth fish scales on top. A shark tooth was mounted on the Instron 3342 load frame and penetrated the exposed area of the two overlapped scales at a displacement rate of 0.1 mm s^{-1}. The nature of the damage in the upper fish scale was subsequently examined in the SEM (FEI, Hillsboro, OR).

Crack Propagation Observations: Crack propagation studies were performed on 2.5-mm wide dog-bone-shaped tensile samples containing a notch of width 1 mm that was cut using a surgical blade. Uniaxial tensile tests were carried out on an Instron 3342 mechanical testing machine (Instron Corp., Norwich, MA) with a load cell of 500 N at a strain rate of 10^{-3} s^{-1} immediately after the removal of the samples from deionized water, where they were kept prior to testing. Engineering stress–strain curves were obtained before the tests were stopped at a maximum strain of 0.143. The specimens were then removed from the Instron machine and immediately immersed into 2.5% glutaraldehyde solution to fix the deformed structure at the fractured region, following with the same procedure described in the structural characterization section.

Uniaxial Tensile Testing: Using a surgical blade, 15 × 3 mm dog-bone-shaped tensile samples were cut in two orientations from the scales with thickness of 0.26–0.53 mm. The variation of thickness is caused by the scales taken from different parts of fish body. However, within one given specimen, the variation of thickness along the gauge length of the sample was deemed to be is 0.42±0.02 mm. In order to prevent slippage, the ends of the samples were glued between sand paper sheets using cyanoacrylate glue, resulting in a gauge length of 8 mm. Uniaxial tensile tests were carried out on an Instron 3342 mechanical testing machine (Instron Corp., Norwich, MA) with a load cell of 500 N at a strain rate of 10^{-3} s^{-1} immediately following the removal of samples from fresh water, where they were kept prior to testing. The tensile results were expressed in terms of engineering stress–strain curves.

In Situ Observations Under Tensile Loading: To verify the deformation mechanisms during the tensile test of notched specimens, dog-bone-shaped tension samples, with a gauge length of 6 mm and width of 4 mm, were prepared in the longitudinal direction. Before testing, a ≈2-mm long pre-crack was made using a new razor blade in each sample. Uniaxial tension tests were performed at 25 °C in an environmental Hitachi S-4300SE/N (Hitachi America, Pleasanton, CA) SEM. Before the sample preparation, the scales were soaked in water for at least 24 h and the prepared samples were kept in water prior to testing. Testing was performed at a displacement rate of 0.5 mm min^{-1} using a Gatan Microtest 150 N bending stage (Gatan, Abington, UK) inside the SEM. Such in situ testing, however, was used specifically to examine crack trajectories and associated deformation and fracture mechanisms, as the excessive deformation during testing and relaxation during imaging made the precise measurement of the load and displacements unreliable. The dehydration of in situ samples tested in tension in the SEM cannot be controlled in the system as it can only run at a vacuum of 10^{-4} Pa. Using estimates based on the fractional weight change, the degree of dehydration in transferring the samples from an isopropanol environment to the SEM, was ≈40%–50%, whereas from a room environment to the SEM it was ≈15%, which is significant dehydration compared to ex situ tension tests where the samples were preserved in water.

Fracture Toughness K_{Ic} Measurements: The K_{Ic} fracture toughness of coelacanth scales was measured using the set-up illustrated in Movie S1 in the Supporting Information. Pre-cracked compact-tension specimens were prepared from the scales and were glued with sand paper onto pressure grips and mounted on an Instron 3342 mechanical testing machine (Instron Corp., Norwich, MA) with a load cell of 500 N. The tests were conducted at a strain rate of 5×10^{-3} s^{-1} with anti-buckling plates. K_{Ic} values were determined in accordance with ASTM Standard E1820 for fracture toughness testing.

In Situ Small-Angle X-Ray Scattering During Mechanical Testing: Using the same preparation procedures as for the dog-bone-shaped tension samples, samples comprising complete scales and those where the mineral layer had been removed were cut from the fully hydrated coelacanth scales in the longitudinal direction. The specimens were loaded in tension, while being simultaneously exposed to synchrotron X-rays at beamline 7.3.3 in the Advanced Light Source synchrotron radiation facility (Lawrence Berkeley National Laboratory, Berkeley, CA, USA). The tensile tests were performed in a Linkam TST-350 stage with a 45-N load cell (Omega, LC703-10) to measure the force. Such an experimental set-up allows for SAXS data collection to be recorded in real time with the measurement of the load–displacement curve. The mechanical tests were performed at room temperature at a displacement rate of 1.4×10^{-2} mm s^{-1}.

A Pilatus 2M detector (Dectris Ltd., Baden, Switzerland) was used to collect the SAXS data. The detector was located at the largest allowable distance, around 4 m from the sample, to detect fine changes in the collagen peak's position. The sample was exposed to X-rays for 0.5 s with intervals of ≈5 s during the mechanical test; this radiation dosage was sufficiently low so as not to affect the structure and properties of the collagen and mineral in the scales.[38]

Quantification of Fibril Orientation Using SAXS: Since the collagenous lamellae have numerous orientations in the coelacanth scale, it is difficult to separate the diffraction arcs in the SAXS data. Instead, 360 even sectors were made on the Debye rings with a span of 1° each, starting from $\Psi = 0°$ to 360°. The sector graph was generated by the polar transformation of the 2D diffraction pattern using the software IGOR Pro (Wavemetrics) in conjunction with the custom macro NIKA (Jan Ilavsky, Argonne National Laboratory, IL, USA). Based on the obtained square map of intensity versus pixel, the 1D graphs, specifically the plots of the integrated intensity as a function of azimuthal angle, were created by using the "Image line profile" tool in NIKA.

Quantification of Fibril Strains: The strain of the collagen fibrils in the lamellae was measured from the X-ray data in terms of the change in 1D peak position determined from the plot of integrated diffraction intensity as a function of *d*-spacing. By using the same software employed in the quantification of fibril orientations, the sample detector distance and beam center were calibrated with the 2D diffraction pattern of a silver behenate standard. In order to convert the 2D SAXS data to 1D peaks, 17 sectors were evenly made on the upper half of the Debye rings, starting from $\Psi = -5°$ to 165°, with a span of 10° in each sector, and then the integrated intensity over the diffraction arc in each sector was radially averaged to obtain the relationship between the intensity peaks and the radial distance of the arc, *q*. Based on the numerical relationship between *q* and the *d*-spacing, plots of integrated intensity as a function of the *d*-spacing for all 17 sectors were generated by the software; intensity peaks were fit to an exponential Gaussian function and a linear background to precisely locate the peak positions. The strain in the collagen fibrils was measured as the change in position of the center of the first-order collagen peak, normalized by the strain in the unstressed state.

Supporting Information

Supporting Information is available from the Wiley Online Library or from the author.

Acknowledgements

H.Q. and W.Y. contributed equally to this work. This work was supported by a Multi-University Research Initiative from the Air Force Office of Scientific Research (AFOSR-FA9550-15-1-0009) to the University of

California Riverside, specifically, through subcontracts to the University of California Berkeley and the University of California San Diego. We acknowledge the use of beamline 7.3.3 at the Advanced Light Source at the Lawrence Berkeley National Laboratory, which is supported by the Office of Science, Office of Basic Energy Sciences, and Division of Materials Sciences and Engineering of the US Department of Energy under Contract no. DE-AC02-05CH11231. We thank Phil Hastings and H. J. Walker from Scripps Institute of Oceanography at UCSD for providing the scales of a preserved coelacanth. We gratefully acknowledge Mason Mackey for helping to us prepare the TEM samples and thank Eric Bushong for helping us with the Micro-CT scan. We also thank Dr. Claire Acevedo for her help with the SAXS experiments and Dr. Elizabeth A. Zimmermann and Dr. Zhijian Wang for their input and discussion on the SAXS data analysis. We appreciate the help from Gaoge Xu on scheme drawing using Solidworks, and input from Xudong Liang and Shiteng Zhao for discussions on the modeling.

Conflict of Interest

The authors declare no conflict of interest.

Keywords

Bouligand structure, coelacanth, fish scales, SAXS, toughening mechanisms

Received: June 19, 2018
Revised: August 24, 2018
Published online:

[1] M. A. Meyers, J. McKittrick, P. Y. Chen, *Science* **2013**, *339*, 773.
[2] R. O. Ritchie, *Nat. Mater.* **2011**, *10*, 817.
[3] J. Y. Sire, P. C. J. Donoghue, M. K. Vickaryous, *J. Anat.* **2009**, *214*, 409.
[4] W. Yang, I. H. Chen, B. Gludovatz, E. A. Zimmermann, R. O. Ritchie, M. A. Meyers, *Adv. Mater.* **2013**, *25*, 31.
[5] R. H. Denison, *Clin. Orthopaed. Relat. Res.* **1963**, *31*, 141.
[6] B. J. F. Bruet, J. H. Song, M. C. Boyce, C. Ortiz, *Nat. Mater.* **2008**, *7*, 748.
[7] D. O. Wagner, P. Aspenberg, *Acta Orthopaedica*. **2011**, *82*, 393.
[8] W. Yang, B. Gludovatz, E. A. Zimmermann, H. A. Bale, R. O. Ritchie, M. A. Meyers, *Acta Biomater.* **2013**, *9*, 5876.
[9] V. R. Sherman, H. C. Quan, W. Yang, R. O. Ritchie, M. A. Meyers, *J. Mech. Behav. Biomed. Mater.* **2017**, *73*, 1.
[10] M. Roberto, F. Barthelat, *Bioinsp. Biomim.* **2016**, *11*, 066001.
[11] V. R. Sherman, N. A. Yaraghi, D. Kisailus, M. A. Meyers, *J. R. Soc. Interface* **2016**, *13*, 20160595.
[12] A. A. Schonborner, G. Boivin, C. A. Baud, *Cell Tissue Res.* **1979**, *202*, 203.
[13] G. A. Brown, S. R. Wellings, *Z. Zellfor.Mikrosk. Anatom.* **1970**, *103*, 149.
[14] A. K. Dastjerdi, F. Barthelat, *J. Mech. Behav. Biomed. Mater.* **2015**, *52*, 95.
[15] E. A. Zimmermann, B. Gludovatz, E. Schaible, N. K. N. Dave, W. Yang, M. A. Meyers, R. O. Ritchie, *Nat. Commun.* **2013**, *4*, 7.
[16] D. J. Zhu, L. Szewciw, F. Vernerey, F. Barthelat, *J. Mech. Behav. Biomed. Mater.* **2013**, *24*, 30.
[17] D. J. Zhu, C. F. Ortega, R. Motamedi, L. Szewciw, F. Vernerey, F. Barthelat, *Adv. Eng. Mater.* **2012**, *14*, B185.
[18] W. Yang, V. R. Sherman, B. Gludovatz, M. Mackey, E. A. Zimmermann, E. H. Chang, E. Schaible, Z. Qin, M. J. Buehler, R. O. Ritchie, M. A. Meyers, *Acta Biomater.*. **2014**, *10*, 3599.
[19] F. G. Torres, M. Malasquez, O. P. Troncoso, *Mater. Sci. Eng. C* **2015**, *51*, 153.
[20] S. Murcia, E. Lavoie, T. Linley, A. Devaraj, E. A. Ossa, D. Arola, *J. Mech. Behav. Biomed. Mater.* **2017**, *73*, 17.
[21] J. L. B. Smith, *Nature* **1939**, *143*, 455.
[22] P. L. Forey, *Nature* **1988**, *336*, 727.
[23] C. T. Amemiya, J. Alfoldi, A. P. Lee, S. H. Fan, H. Philippe, I. MacCallum, I. Braasch, T. Manousaki, I. Schneider, N. Rohner, C. Organ, D. Chalopin, J. J. Smith, M. Robinson, R. A. Dorrington, M. Gerdol, B. Aken, M. A. Biscotti, M. Barucca, D. Baurain, A. M. Berlin, G. L. Blatch, F. Buonocore, T. Burmester, M. S. Campbell, A. Canapa, J. P. Cannon, A. Christoffels, G. De Moro, A. L. Edkins, L. Fan, A. M. Fausto, N. Feiner, M. Forconi, J. Gamieldien, S. Gnerre, A. Gnirke, J. V. Goldstone, W. Haerty, M. E. Hahn, U. Hesse, S. Hoffmann, J. Johnson, S. I. Karchner, S. Kuraku, M. Lara, J. Z. Levin, G. W. Litman, E. Mauceli, T. Miyake, M. G. Mueller, D. R. Nelson, A. Nitsche, E. Olmo, T. Ota, A. Pallavicini, S. Panji, B. Picone, C. P. Ponting, S. J. Prohaska, D. Przybylski, N. R. Saha, V. Ravi, F. J. Ribeiro, T. Sauka-Spengler, G. Scapigliati, S. M. J. Searle, T. Sharpe, O. Simakov, P. F. Stadler, J. J. Stegeman, K. Sumiyama, D. Tabbaa, H. Tafer, J. Turner-Maier, P. van Heusden, S. White, L. Williams, M. Yandell, H. Brinkmann, J. N. Volff, C. J. Tabin, N. Shubin, M. Schartl, D. B. Jaffe, J. H. Postlethwait, B. Venkatesh, F. Di Palma, E. S. Lander, A. Meyer, K. Lindblad-Toh, *Nature* **2013**, *496*, 311.
[24] S. B. Hedges, C. A. Hass, L. R. Maxson, *Nature* **1993**, *363*, 501.
[25] J. L. Smith, *Nature* **1953**, *171*, 99.
[26] J. L. B. Smith, *Nature* **1955**, *176*, 473.
[27] H. Fricke, K. Hissmann, *Nature* **1990**, *346*, 323.
[28] J. Millot, *Nature* **1954**, *174*, 426.
[29] J. A. Musick, M. N. Bruton, E. K. Balon, *The Biology of Latimeria Chalumnae and Evolution of Coelacanths*, Kluwer Academic Publishers, Dordrecht; Boston **1991**.
[30] J. Millot, *Nature* **1955**, *175*, 362.
[31] M. Smith, *J. Zool.* **1972**, *167*, 501.
[32] F. J. Meunier, L. Zylberberg, *Indopacific Fish Conference*, Societé Française Ichtyologie, Paris **1999**.
[33] R. Puxkandl, I. Zizak, O. Paris, J. Keckes, W. Tesch, S. Bernstorff, P. Purslow, P. Fratzl, *Phil. Trans. R. Soc. B: Biol. Sci.* **2002**, *357*, 191.
[34] H. S. Gupta, J. Seto, W. Wagermaier, P. Zaslansky, P. Boesecke, P. Fratzl, *Proc. Natl. Acad. Sci. USA* **2006**, *103*, 17741.
[35] A. Bigi, M. Burghammer, R. Falconi, M. H. J. Koch, S. Panzavolta, C. Riekel, *J. Struct. Biol.* **2001**, *136*, 137.
[36] A. Hexemer, W. Bras, J. Glossinger, E. Schaible, E. Gann, R. Kirian, A. MacDowell, M. Church, B. Rude, H. Padmore, in *XIV International Conference on Small-Angle Scattering*, Vol. *247*, IOP Publishing Ltd, Bristol **2010**.
[37] E. A. Zimmermann, E. Schaible, H. Bale, H. D. Barth, S. Y. Tang, P. Reichert, B. Busse, T. Alliston, J. W. Ager, R. O. Ritchie, *Proc. Natl. Acad. Sci. USA* **2012**, *109*, 13022.
[38] H. D. Barth, E. A. Zimmermann, E. Schaible, S. Y. Tang, T. Alliston, R. O. Ritchie, *Biomaterials* **2011**, *32*, 8892.

